12-27-2021

Case Studies of Atmospheric River-Induced Surface Changes in the Arctic

Yonghuai Huang

Case Studies of Atmospheric River-Induced Surface Changes in the Arctic

Yonghuai Huang

Geodata Science for Professionals MS Program '
Department of Earth, Atmospheric, and Planetary Sciences '
Purdue University '

Abstract

Atmospheric river (AR) takes a significant role in transporting warm moisture into the Arctic, which could further enhance the Arctic Amplification. This project aims to examine the surface conditions during selected cases of AR events that are detected by climate time series of Arctic AR index. Mono-level variables related to temperature, pressure, heat fluxes and wind speed of fourteen AR events were analyzed using the MERRA-2 derived Arctic AR index, and results were compared with the detected AR basins. Results of MERRA-2 data show that AR basins detected by both Integrated Water Vapor (IWV) and Integrated water Vapor Transport (IVT) indices were able to capture changes on the surface conditions caused by Arctic AR intrusions. Evolution of AR was characterized best by surface temperature, when the location of an AR basin was tracked by the low-pressure field. Latent and sensible heat fluxes showed that evaporation dominated when ARs moved over ocean, but the mechanism and effect of it remained in questions. Also, the combination of longwave fluxes at the surface and atmosphere proved the fact that AR intrusion did enhance the Greenhouse Effect in the Arctic region. The IVT-based AR index had better performance in capturing the movement of ARs than the IWV-based index did, and the overall performance of AR indices was impacted by factors such as seasonal effect and extreme background value over continents, which should be considered for future research.

1. Introduction

An atmospheric river (AR) is a long, narrow filaments of enhanced water vapor transport that is typically associated with a low-level jet and extratropical cyclone (Ralph et al., 2019). Previous studies have stated that ARs can produce large amounts of precipitation when they make land-fall, thus serving as a moisture source to many regions (Baggett et al., 2016; Guan et al., 2010; Nash et al., 2018). Atmospheric rivers also contribute to a great portion of extreme precipitation and flooding events across the world (Mix et al., 2019; Sodemann et al., 2020; Waliser & Guan, 2017). Most importantly, ARs help to maintain the energy and moisture balance between high and low latitudes (Guan et al., 2010; Hegyi & Taylor, 2018; Liu et al., 2018).

The Arctic region has warmed at rates doubling the global average over the past decades, a phenomenon known as Arctic Amplification (Cohen et al., 2014). It has obvious features such as rapid warming, associated sea-ice decline, and glacier retreat in the Arctic area (Crépin et al., 2017), which have significant ecological and economic impacts locally and globally (Cohen et al., 2014; Crépin et al., 2017; Graversen & Burtu, 2016). Previous studies have examined many processes that can enhance Arctic Amplification. Among those processes, increased poleward moisture transport has been found contributing to Arctic warming and sea ice decline due to the physical process of cloud radiative forcing produced by water vapor, cloud formation, and cloud properties (Johansson et al., 2017; Liu et al., 2018; Woods & Caballero, 2016). And, one major mechanism responsible for atmospheric water vapor transport from lower latitudes is the atmospheric river (Baggett et al., 2016; Dufour et al., 2016; Gimeno et al., 2019; Naakka et al., 2019; Nash et al., 2018; Nygård et al., 2020).

On the one hand, atmospheric rivers carry warm moisture into the Arctic, which accounts for over 90% of the total poleward moisture transport in the mid-latitudes (Zhu & Newell, 1998). The heat brought into the Arctic by the ARs is found to be associated with an averaged surface warming up to 5 K in the winter and 2 K in the summer (Johansson et al., 2017). In synergy with the synoptic-scale wave, AR surface warming can

amplify planetary-scale wave that transports sensible and latent heat poleward and further enhances the downward infrared radiation (Baggett et al., 2016). On the other hand, by adding a warm moisture layer between the sea ice and the Arctic atmosphere from above, the extra heat provided by the layer could warm up the air above it, so that this heating drives increased buoyancy and further strengthens the ascent and heating of the mid-troposphere (Komatsu et al., 2018). This bottom layer of amplified warm moisture intrusion can also change the state of local atmosphere structure, such as cloudiness and stability, and persists for many days after the AR passed (Johansson et al., 2017; Woods & Caballero, 2016). Therefore, the atmospheric river plays a significant role in affecting the surface conditions of the Arctic region and enhancement of the Arctic Amplification.

Previous studies have developed systematic methods for identifying different AR events (Ralph et al., 2019; Rutz et al., 2019; Shields et al., 2018). Two common moisture measurements for AR detection are Integrated Water Vapor (IWV) and Integrated Water Vapor Transport (IVT) (Rutz et al., 2019; Shields et al., 2018):

$$IWV = -\frac{1}{g}\int_{10002}^{00} q(p)dp, \text{ and}$$

$$IVT = -\frac{1}{g}\int_{10002}^{00} q(p)|V_h(p)|dp,$$

where q is the specific humidity in kg/kg; p is pressure in hPa; g is gravitational acceleration, which equals to 9.8 m/s^2; and Vh = (u, v), with u and v being zonal and meridional winds, respectively. Zhang et al. (2021a) created a multifactorial algorithm with moisture fields (IWV, IVT or IWV + IVT), climatological thresholds, shape criteria, and temporal thresholds applied to the NASA MERRA-2 data for ARTMIP (NCAR CDG, 2019) and generated the new AR indices for the US West Coast and the Midwest by using the R-DeltaRho software with the Hadoop system. Their paper stated that IWV-based AR indices identify the longest AR event duration and most accumulated precipitation. On the other hand, IVT-based AR indices can capture the accumulation of intense orographic precipitation. Zhang then applied modified AR detection algorithm to the Arctic reanalysis

data to generate the Arctic AR index, from which all detected AR basins studied in this project are produced (Zhang et al., 2021b).

As stated in the interim report, the goal of this project was to examine and analyze surface conditions within the same area and time period of selected AR cases and characterize, if any, atmospheric and air-surface flux changes potentially attributed to the AR events detected by this climate time series Arctic AR index with unknown performance. This report aimed to examine the consistency of AR-correlated changes that were observed in previous case study and summarize results of further research after the interim report.

2. Data

The primary dataset used in this project is the version 5.12.4 of Modern-Era Retrospective analysis for Research and Applications, version 2 (MERRA-2) reanalysis data (Gelaro et al., 2017), from which the Arctic AR indices are developed upon. This dataset has global coverage with spatial resolution of 0.5º latitude x 0.625º longitude and temporal range from 1980 to present, with hourly resolution. Since previous case study had analyzed mono-level data, including 2-meter temperature, latent heat flux and sensible heat flux, this report primarily focused on 12 mono-level variables, with 10 other variables which were used as supplementary materials for plotting (Table.1). However, since the integration model of radiation field in MERRA-2 dataset did not remove the shortwave source at nighttime in the Arctic region, plots of both shortwave fluxes were not informative enough, and thus were excluded from this report.

Primary	supplementary
2-meter temperature	2-meter specific humidity
geopotential at 1000 hPa	surface pressure
net downward longwave flux at surface	wind (U&V) at 2-meter
upwelling longwave flux at top of atmosphere	geopotential at 850 hPa
net downward shortwave flux at surface	geopotential at 500 hPa
net downward shortwave flux at top of atmosphere	total precipitable water vapor
latent heat flux	temperature at 850 hPa
sensible heat flux	specific humidity at 850 hPa
wind (U&V) at 850 hPa	sea-level pressure
wind (U&V) at 500 hPa	

Table. 1. Mono-level variables of MERRA-2 dataset used in this research. For plots of supplementary variables, please check Appendix III.

This study used Arctic AR index created by Zhang et al. (2021b), who modified the AR detection algorithm in (Zhang et al., 2021a) for detection and tracking in the Arctic region. The region was defined as the area above 60º N latitude in this project. The AR index created with the 95th climatological threshold, 1500-km geometry threshold, and 12-hour temporal persistence threshold applied to both IVT and IWV moisture fields from the MERRA-2 data for ARTMIP (NCAR CDG, 2019) were chosen for this study. With these Arctic AR indices, this research preliminarily surveyed significant "circumpolar" AR cases in the Arctic region from 1980 to 2019 and produced time series plots of these AR basins. Due to the large data size and long analysis time for each individual AR case, as well as the attempting purpose of this project, only 14 AR cases in 2018 were selected and analyzed in this preliminary study. Among these 14 cases, 7 AR events were in January & February, and 7 events were in September, which was the time of sea ice minimum in the Arctic region. AR events were also selected in purpose of comparing regional difference in ARs' impact on the surface condition (e.g., Greenland, land bridge, central Arctic Ocean etc.) and difference in performance between IVT & IWV indices.

3. Methods

Data of mono-level variables in radiation, surface flux and single-level field within the same duration time of corresponding AR events were extracted from MERRA-2 datasets using R. Hourly data from 2010 to 2019 were imported to calculate decadal mean value of each variable at each grid point. Then the decadal mean was removed from data corresponding to specific time frame and AR basin to generate data frames for individual AR event. For each AR event, time series polar projection heatmap of an individual variable was created for visualization as well as comparison with a plot of AR basin, which was also produced in a similar procedure with the Arctic AR index. AR basins and selected variables were plotted in every three hours throughout the duration of detected AR events, which provided a series of AR basins plots (Appendix I) that variables plots (Appendix II) could be referred to. Due to the large data size and long computing time, most plots were generated using the Simple Linux Utility for Resource Management (SLURM) on Purdue's High Performance Computing Bell cluster.

4. Results

4.1. Surface Temperature

Significant increase in surface temperature was detected throughout the AR events, especially for those in winter. Similar to the temperature change found in previous case studies, the impacted areas overlapped entirely with the detected AR basins. According to plots of winter AR events, surface temperature showed an increase around 10 K comparing to the decadal mean value in the area corresponding to detected AR basins, when some AR events even had higher increase (< 20 K) near the leading edge of the AR basin (Fig. 1). For example, the AR basin of AR event 10023 moved from southeast to Greenland all the way up to Svalbard. It was clear that surface temperature was higher than the surrounding environment and had its maximum band (~ 20 K) at the leading edge of the AR basin, which located between Greenland and Svalbard at 0 AM, 2018-01-13. The overall magnitude of temperature change only varied from one to two units after expanding or contracting of AR basins, and remained consistent along the track of AR basins' movement.

Besides, some AR events also showed decreases in magnitude of temperature change during the last 3 to 6 hours of events (Fig. 2). Therefore, the change in surface temperature could indicate the evolving of AR basins. Since the surrounding surface temperature was about 20 K comparing to the decadal mean in summer, the temperature change caused by AR was not detectable in most September AR events.

The temperature pattern also changed as the AR basin moved into different regions. Significantly lower magnitude in surface temperature's increase were observed when ARs moved into the central Arctic Ocean or the land bridge/continent. For instance, AR event 10023 showed a clear boundary between the temperature impacted area and the central Arctic Ocean (Fig. 3), where the high temperature profile spread out eastward and westward when the AR moved norther toward the pole, indicating the existence of a potential resistant in the central Arctic Ocean. AR event 10033 also showed that the temperature change was highly influenced by the cold background near the land bridge (Fig. 4). When the AR moved from the Pacific Ocean to the Arctic Ocean across Siberia, the extremely cold surrounding environment (< -20 K) resulted in a surface temperature gradient inside the AR. Although the overall surface temperature was higher inside the basin, there was still a gradient where temperature at the center was highest, and lower toward the edge of the basin. In contrast, some AR events showed increases of surface temperature in the center or across the AR basin through time. AR event 10021 was a good example showing the heat supply around Barents Sea during the middle stage of the AR event (Fig. 5).

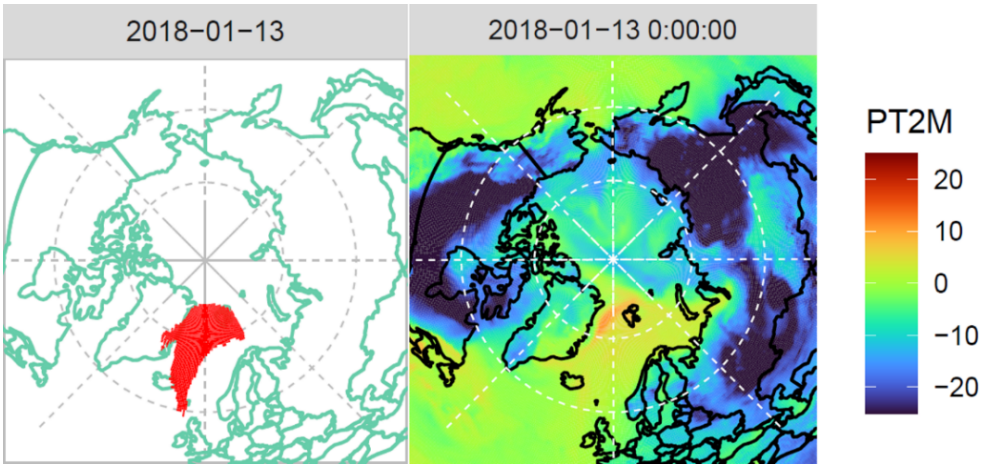

Fig. 1. Polar projection of AR basin (left, red shade) and heat map of surface temperature (right, unit in K) of the MERRA-2 AR 10023 event (2018-01-12 to 2018-01-13) at time step 2018-01-13 0:00. Surface temperature in the area corresponding to the AR basin was about 10 K higher than the surrounding, which reached its maximum in the area between Greenland and Svalbard. The AR basin was originally in southeast to Greenland, then moved toward the Central Arctic Ocean. For more details about the AR basin, please check Appendix I.

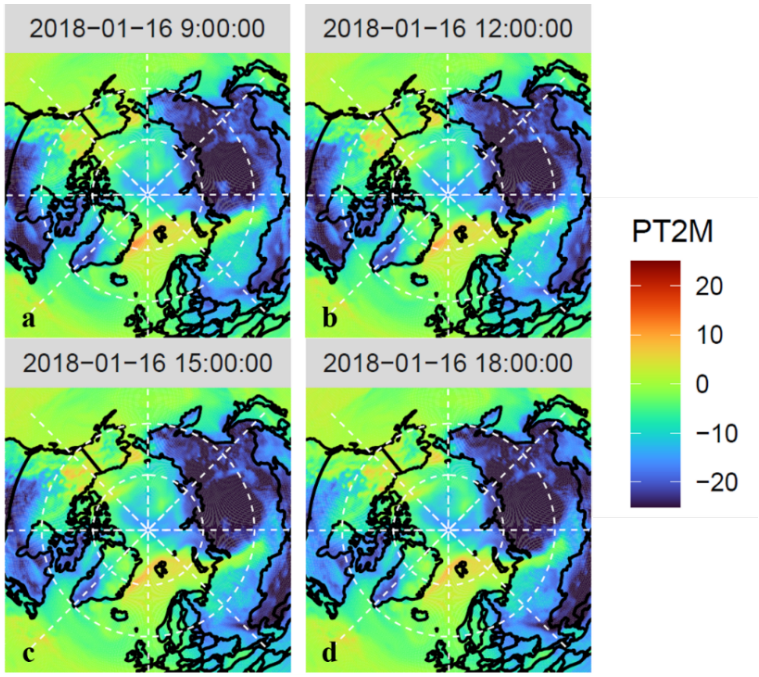

Fig. 2. Heat maps of surface temperature (unit in K) of the MERRA-2 AR 10021 event (2018-01-09 to 2018-01-16) at time step (a) 2018-01-16 9:00, (b) 2018-01-16 12:00, (c) 2018-01-16 15:00, and (d) 2018-01-16 18:00. In this case, the detected AR basin located between Greenland and Eurasia, crossing the Svalbard. Surface temperature in the corresponding area, especially the ocean in east to Greenland, decreased from > 20 K to < 10 K throughout the last 6 hours of the event. Please check Appendix I for details about AR basin, and Appendix II for details about the surface temperature.

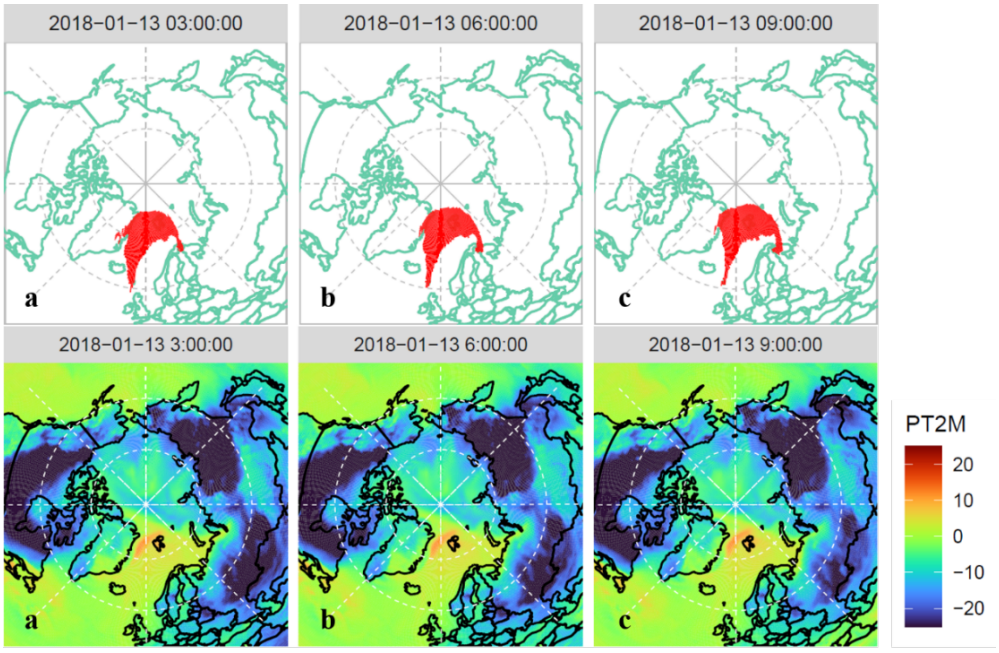

Fig. 3. Polar projections of AR basin (top, red shade) and heat maps of surface temperature (bottom, unit in K) of the MERRA-2 AR 10023 event (2018-01-12 to 2018-01-13) at time step (a) 2018-01-13 3:00, (b) 2018-01-13 6:00, and (c) 2018-01-13 9:00. Instead of keeping moving toward the pole like what the detected AR did in previous time steps, both the basin and surface temperature profile started to spread out laterally when the AR reached the ocean in north to Svalbard. One possible reason was that the AR was not strong enough to penetrate into the cold, high-pressure central Arctic Ocean. Please check Appendix I for details about AR basin, and Appendix II for details about the surface temperature.

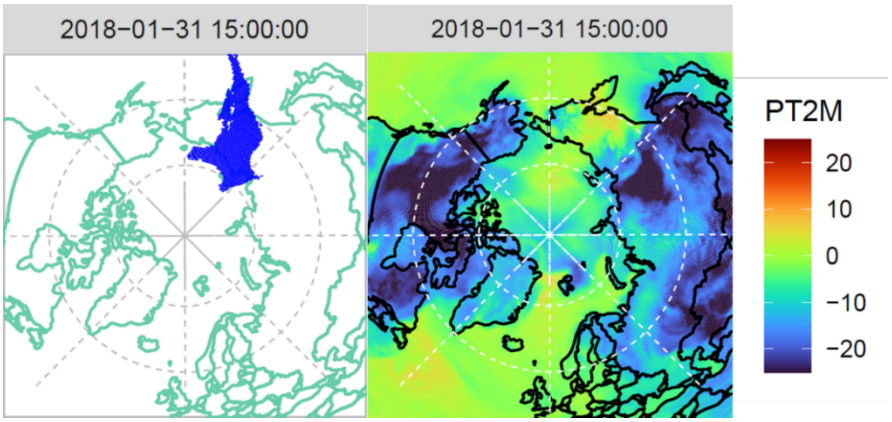

Fig. 4. Polar projection of AR basin (left, blue shade) and heat map of surface temperature (right, unit in K) of the MERRA-2 AR 10033 event (2018-01-31 to 2018-02-03) at time step 2018-01-31 15:00. Surface temperature in the area corresponding to the AR basin was higher than the surrounding, but the magnitude of the change was lower as it got closer to the edge of the AR basin. The surface temperature of surrounding environment was extremely low in this case.

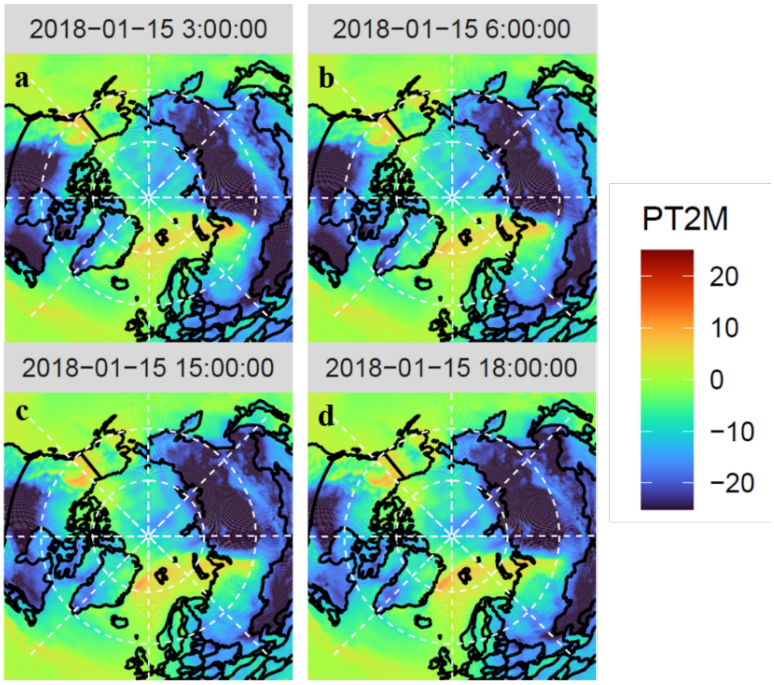

Fig. 5. Heat maps of surface temperature (unit in K) of the MERRA-2 AR 10021 event (2018-01-09 to 2018-01-16) at time step (a) 2018-01-15 3:00, (b) 2018-01-15 6:00, (c) 2018-01-15 15:00, and (d) 2018-01-15 18:00. In this case, the detected AR basin moved from Greenland to Eurasia, crossing the Svalbard. Surface temperature in the corresponding area around Svalbard had increased from < 10 K to < 20 K through time in the middle stage of the AR event. Please check Appendix I for details about AR basin, and Appendix II for details about the surface temperature.

4.2. Geopotential at 1000 hPa

Unlike surface temperature, the geopotential change caused by AR intrusion was not consistent as the AR evolved. The geopotential value inside the AR basin varied from -100 to -200 m comparing to the decadal mean, and showed significant decrease in magnitude when AR basins expanded or moved into area with high positive geopotential value, e.g., the continent. AR event 10021 showed that the low-pressure profile did not follow the movement of detected AR basin when the basin moved into northern Eurasia, which had high-pressure background value (~ 300 m) (Fig. 6). In some extreme cases, the geopotential at 1000 hPa at the edge of AR basin was around 0 m, which was equal to the decadal mean (Fig. 7). When the geopotential of surrounding environment was high, the geopotential value inside AR basins could be impacted by the surrounding high value, and

had a lower pressure profile inside the AR basin. In Fig. 8, plots of AR event 10247 showed a mixture of high-low geopotential intervals inside the AR basin when the AR basin crossed the high-pressure land bridge area, which created three separate low-pressure areas inside the basin. However, plots of all 14 selected AR events showed that there was always a low-pressure center (~ -300 m comparing to the decadal mean) to the west or southwest of the AR basin, which also moved as the AR basin did. According to plots of AR event 10662, the low-pressure center initially located near the pole, which was in west to the detected AR basin, when the AR moved from northern Eurasia to the central Arctic Ocean. By the end of the event, the AR retreated back into the northern Eurasia, and the low-pressure center followed its movement to the Kara Sea (Fig. 9). There were exceptions in some events like AR event 10021, a new low-pressure center was generated and followed the track of the AR basin. The latter low-pressure center then merged into the original center and thus created a larger low-pressure center, which amplified the geopotential change inside the AR basin (Fig. 10).

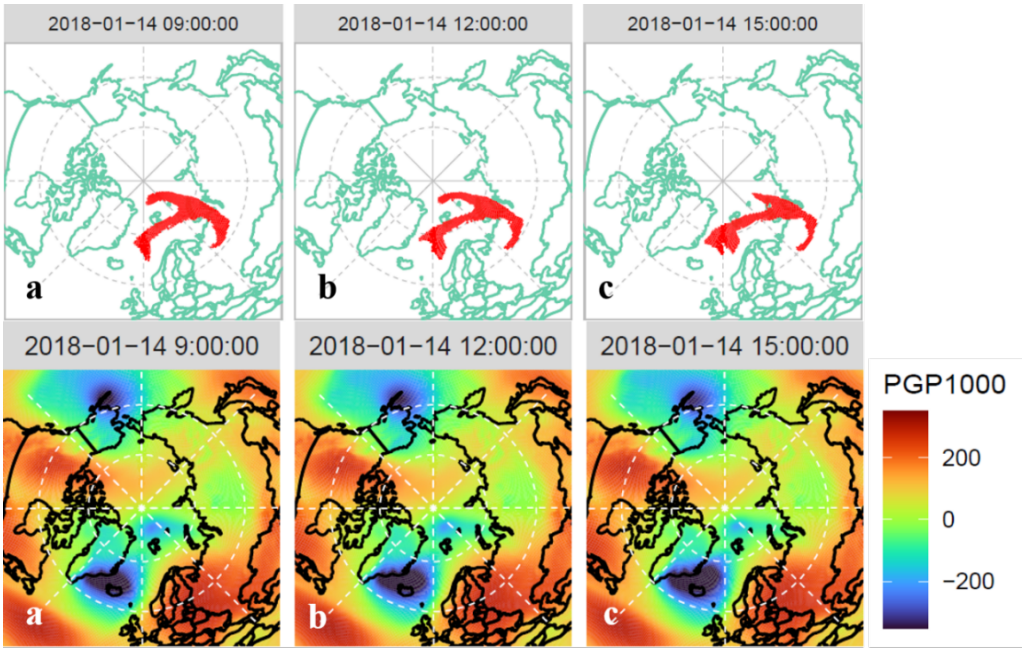

Fig. 6. Polar projections of AR basin (top, red shade) and heat maps of geopotential at 1000 hPa (bottom, unit in m) of the MERRA-2 AR 10021 event (2018-01-09 to 2018-01-16) at time step (a) 2018-01-14 9:00, (b) 2018-01-14 12:00, and (c) 2018-01-14 15:00. The low-pressure center (~ -300 m) was in southwest to the AR basin near the southern Greenland. In this case, the AR moved into

northern Eurasia and curved toward west. However, the low geopotential profile did not penetrate into the continent following the AR basin. Please check Appendix I for details about AR basin, and Appendix II for details about the geopotential at 1000 hPa.

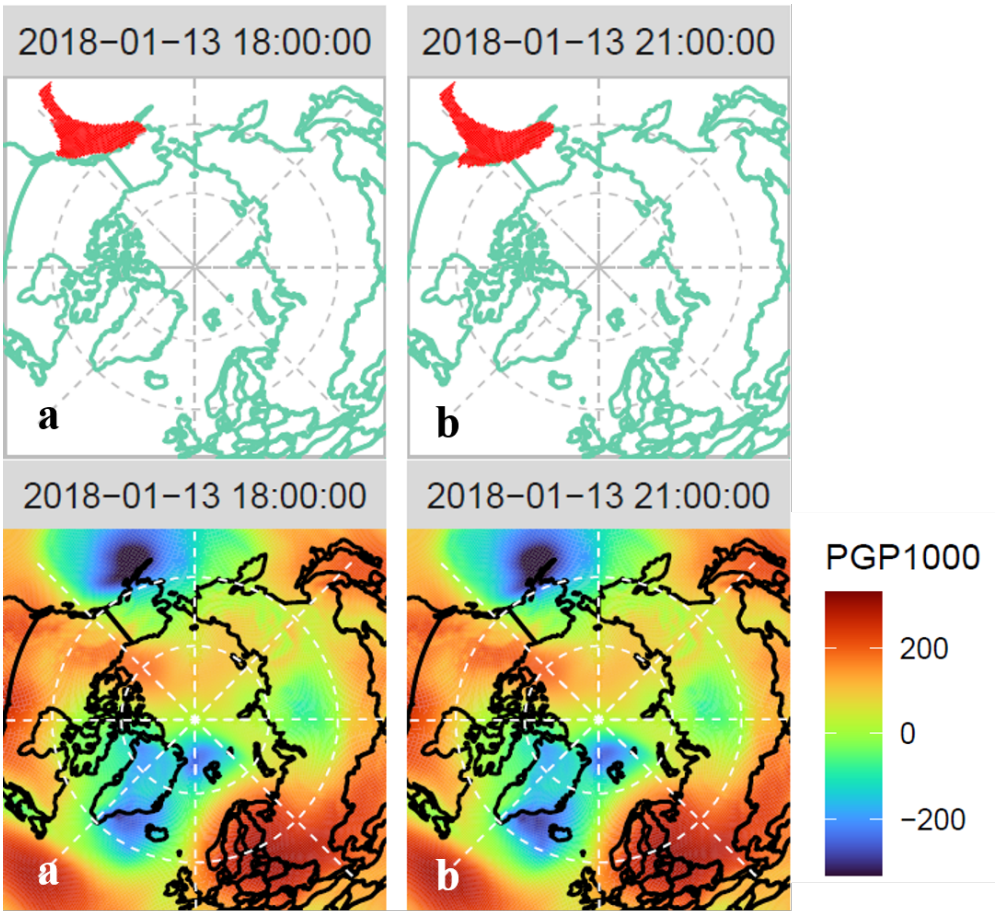

Fig. 7. Polar projections of AR basin (top, red shade) and heat maps of geopotential at 1000 hPa (bottom, unit in m) of the MERRA-2 AR 10440 event (2018-01-13 to 2018-01-17) at time step (a) 2018-01-13 18:00 and (b) 2018-01-13 21:00. The low-pressure center (~ -300 m) was in west to the AR basin near Alaska. In this case, the 1000 hPa geopotential of the detected AR basin was close to 0 m, meaning that it was about the same as the decadal mean. Please check Appendix I for details about AR basin, and Appendix II for details about the geopotential at 1000 hPa.

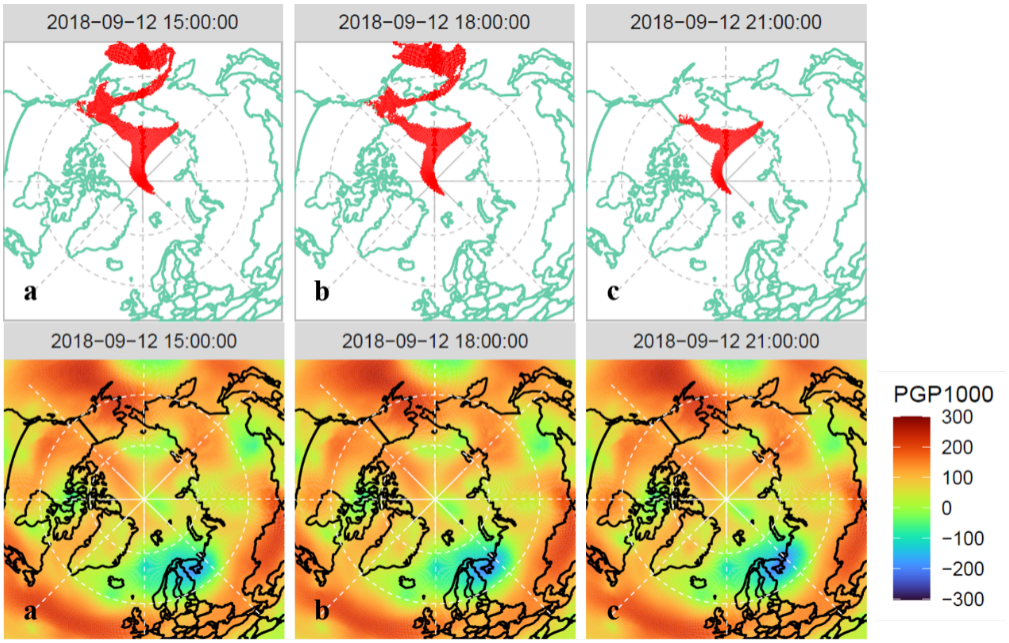

Fig. 8. Polar projections of AR basin (top, red shade) and heat maps of geopotential at 1000 hPa (bottom, unit in m) of the MERRA-2 AR 10247 event (2018-09-11 to 2018-09-14) at time step (a) 2018-01-12 15:00, (b) 2018-01-12 18:00, and (c) 2018-01-12 21:00. The low-pressure profile in the AR basin was close to 0 m, and was cut off by the high-pressure surrounding (~ 300 m), especially near the land bridge area, into three separate parts. Please check Appendix I for details about AR basin, and Appendix II for details about the geopotential at 1000 hPa.

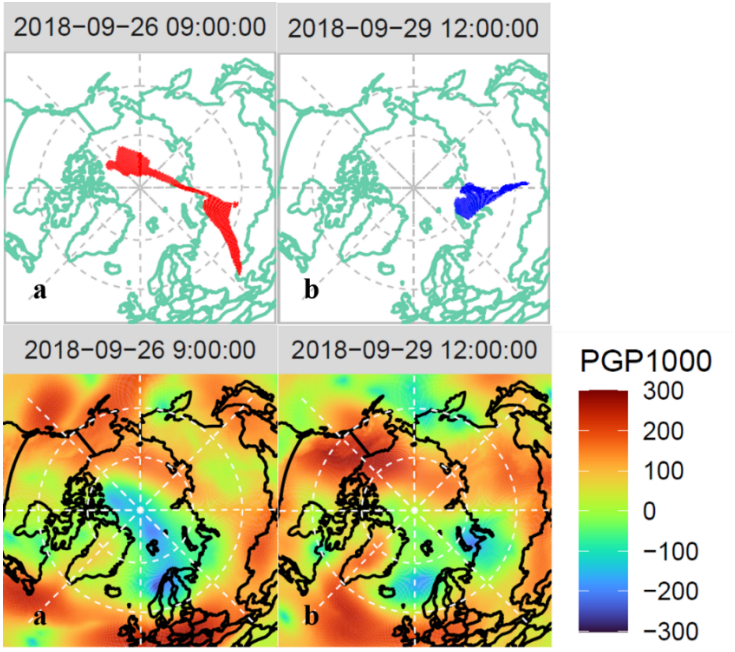

Fig. 9. Polar projections of AR basin (top, red & blue shade) and heat maps of geopotential at 1000 hPa (bottom, unit in m) of the MERRA-2 AR 10662 event (2018-09-25 to 2018-09-30) at time step (a)

2018-09-26 9:00 and (b) 2018-09-29 12:00. At time step (a), as the AR moved from northern Eurasia toward the central Arctic Ocean, the low-pressure center located west to the AR basin, which was the near the pole. As the AR evolved through time, it retreated back to the northern Eurasia at time step (b) and the low-pressure center followed its movement all the way to the Kara Sea.

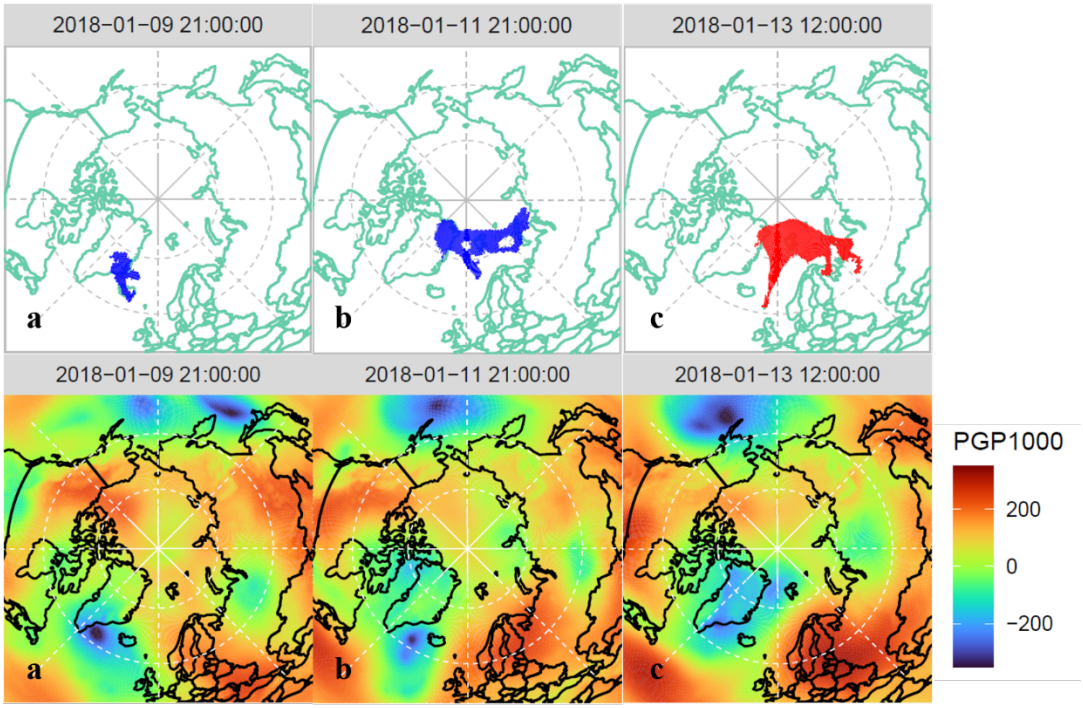

Fig. 10. Polar projections of AR basin (top, blue & red shade) and heat maps of geopotential at 1000 hPa (bottom, unit in m) of the MERRA-2 AR 10021 event (2018-01-09 to 2018-01-16) at time step (a) 2018-01-09 21:00, (b) 2018-01-11 21:00, and (c) 2018-01-13 12:00. At time step (a) the detected AR basin was in southeast to Greenland, and the low-pressure center was in west to it. As the AR moved toward the pole, the low-pressure center also moved northward and reached Baffin Bay at time step (b). However, a new low-pressure was generated in south to the Greenland at the same time and started to move northward along the track of AR. The latter pressure center then merged into the original one and lower the pressure across the whole Greenland area at time step (c). The new "giant" pressure center was still west to the detected AR basin, and amplified the low-pressure profile inside the basin.

4.3. Longwave Fluxes

Plots of selected AR events showed that in the area of AR basins, net downward longwave fluxes at ground surface were about 50 W/m^2 more than the decadal mean, when upwelling longwave fluxes at top of atmosphere was about 100 W/m^2 lower than the decadal mean (Fig. 11). Similar to surface temperature, the change in longwave fluxes were

consistent along the track of ARs' movement, but the longwave profile was not exactly in the shape of the detected basin, which mainly depended on the strength of longwave fluxes of surrounding environment. Also, the surface longwave fluxes plot of AR event 10023 showed the lateral spreading in north to Svalbard similar to what had been observed in surface temperature plots, and thus, there might be a potential heat source effecting the AR movement (Fig. 12). However, pattern of longwave fluxes became unobservable when AR basins moved into continents, so that most observations were made above the Arctic Ocean or islands, e.g., Greenland.

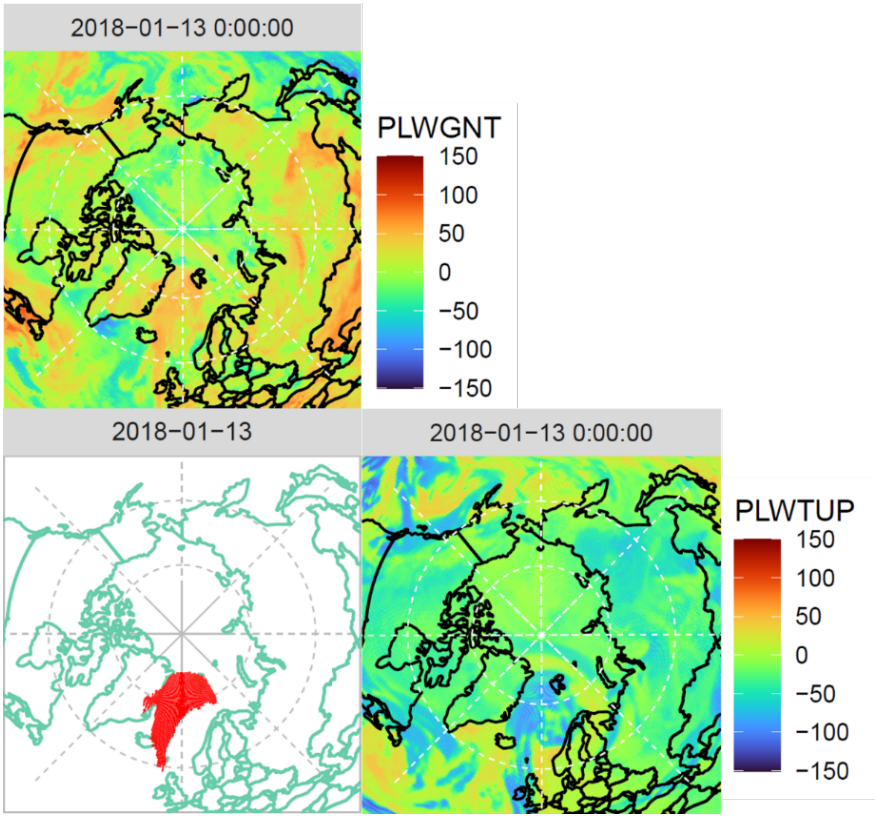

Fig. 11. Polar projections of AR basin (bottom left, red shade), heat maps of net downward longwave fluxes at surface (top, unit in W/m^2), and upwelling longwave flux at top of atmosphere (bottom right, unit in W/m^2) of the MERRA-2 AR 10023 event (2018-01-12 to 2018-01-13) at time step 2018-01-13 0:00. The overall size of net downward surface longwave flux profile was larger than the AR basin, with a value around 50 W/m^2 more than the decadal mean. In contrast, the upwelling top of atmosphere longwave flux was about 100 W/m^2 less than the decadal mean. Please check Appendix I for details about AR basin, and Appendix II for details about net downward longwave fluxes at surface & upwelling longwave fluxes at top of atmosphere.

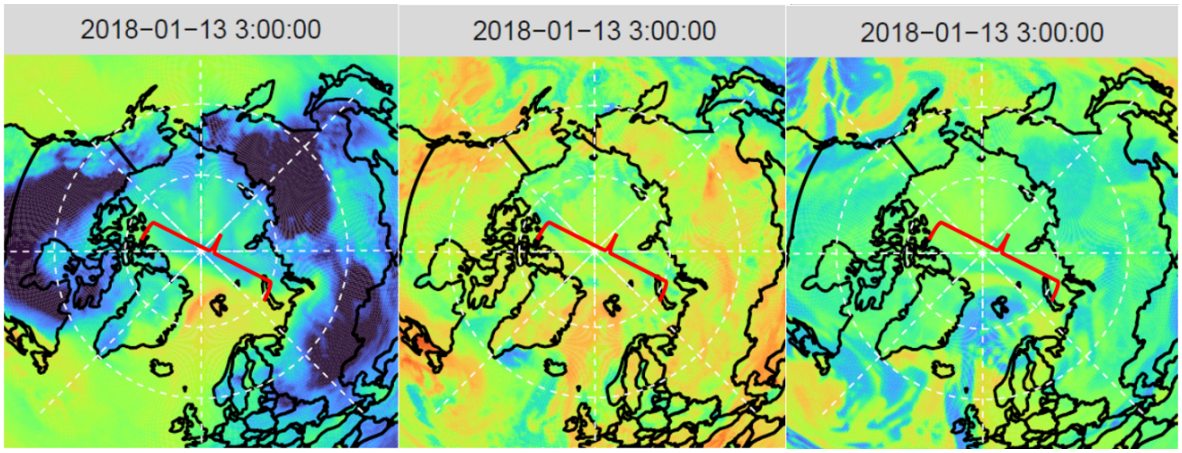

Fig. 12. Heat maps of surface temperature (left, unit in K), net downward longwave fluxes at surface (middle, unit in W/m^2), and upwelling longwave fluxes at top of atmosphere (right, unit in W/m^2) of the MERRA-2 AR 10023 event (2018-01-12 to 2018-01-13) at time step 2018-01-13 3:00. The red bracket highlighted the area that the later spreading located (a band extended from north to the Greenland to west of Kara Sea).

4.4. Latent Heat Flux and Sensible Heat Flux

Land-ocean difference were found in plots of latent heat fluxes. Above the Arctic Ocean, the latent heat flux was around -100 to -150 W/m^2 inside the AR basins, which was in good agreement with the magnitude of negative latent heat fluxes found in previous case studies (Fig. 13). Such pattern was observed across the whole AR basin, with the highest magnitude at the center, which indicated that although evaporation did not cover the entire detected AR basin, it still dominated when atmospheric rivers intruded into the Arctic Ocean. The magnitude of these negative latent heat fluxes generally decreased by the end of the event, or when the AR basin moved into the central Arctic Ocean. For instance, the negative latent heat flux band in plots of AR event 10036 indicated massive evaporation following the AR intrusion, as well as showing a clear path of the AR's movement. However, after the AR reached the central Arctic Ocean, the negative latent heat flux became unobservable, meaning no evaporation beneath the AR near the pole (Fig. 14). On the other hand, when ARs penetrated into Greenland or continents, the value of latent heat flux inside the basin would increase toward zero or even shifted to positive value. The former might indicate the lack of moisture supply on the continents, and the latter was the

result of precipitation due to landfall of atmospheric rivers. According to plots of AR event 10234, when the atmospheric river made its landfall on the Europe at 12pm, 2018-08-04, latent heat flux value of the detected AR basin and the surrounding environment became positive, meaning a massive precipitation along the coastal region (Fig. 15).

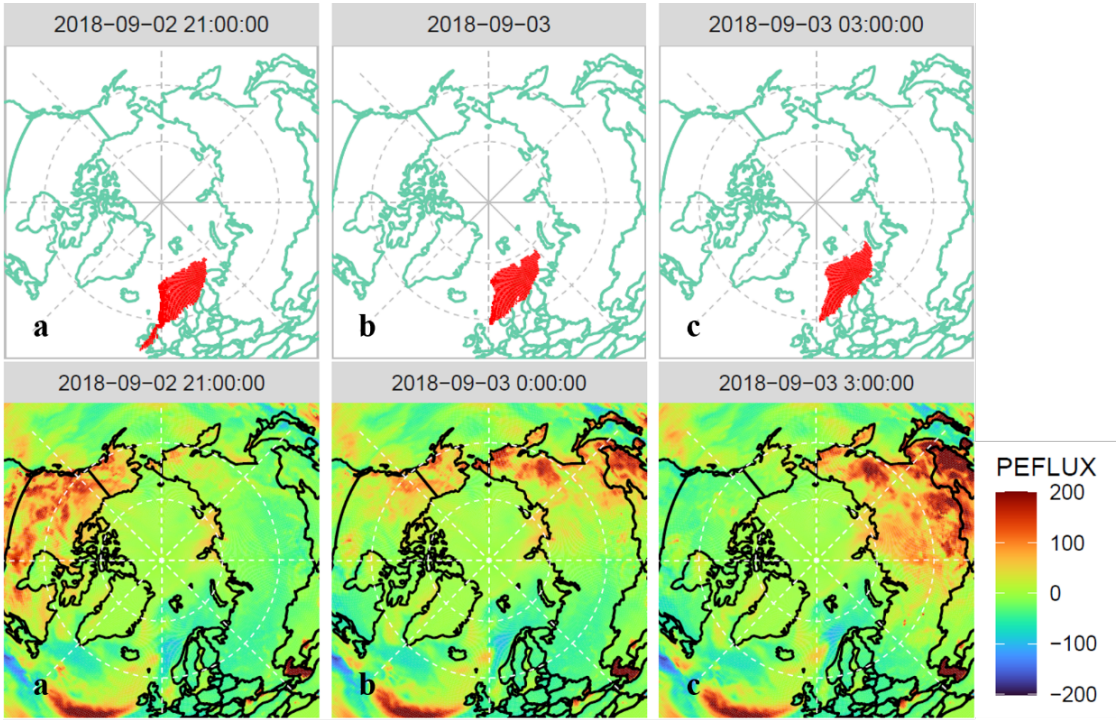

Fig. 13. Polar projections of AR basin (top, red shade) and heat maps of latent heat flux (bottom, unit in W/m^2) of the MERRA-2 AR 10234 event (2018-09-01 to 2018-09-05) at time step (a) 2018-09-02 21:00, (b) 2018-09-03 0:00, and (c) 2018-09-03 3:00. Latent heat flux in the detected AR basin was overall lower than the surrounding environment (which was about 0) and value at the center of the basin was around 150 W/m^2 lower than the decadal mean. However, the impacted area was smaller than the detected AR basin. Please check Appendix I for details about AR basin, and Appendix II for details about latent heat fluxes.

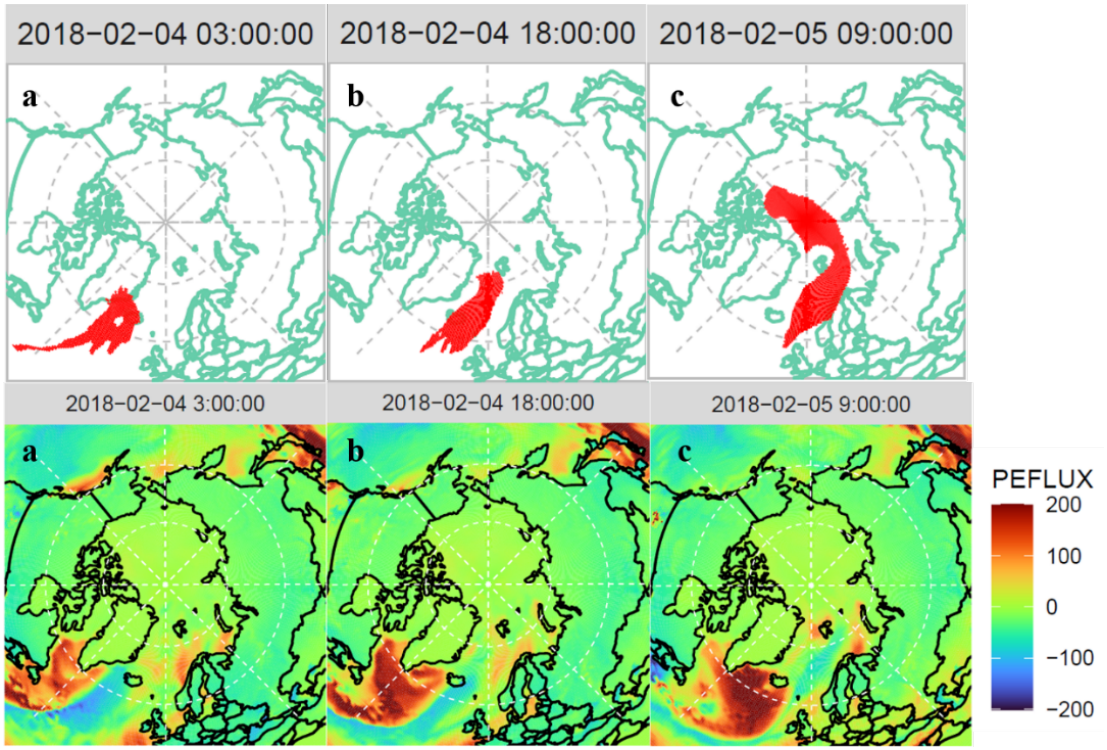

Fig. 14. Polar projections of AR basin (top, red shade) and heat maps of latent heat flux (bottom, unit in W/m^2) of the MERRA-2 AR 10036 event (2018-02-03 to 2018-02-05) at time step (a) 2018-02-04 3:00, (b) 2018-02-04 18:00, and (c) 2018-02-05 9:00. At both time steps (a) and (b), latent heat flux in the detected AR basin showed a clear path of AR movement with value around -100 W/m^2, and the low value profile reached as far as the AR basin did. By the end of the event, the AR basin crossed the pole and went toward Alaska, meanwhile, the low latent heat flux profile became undetectable near the central Arctic Ocean.

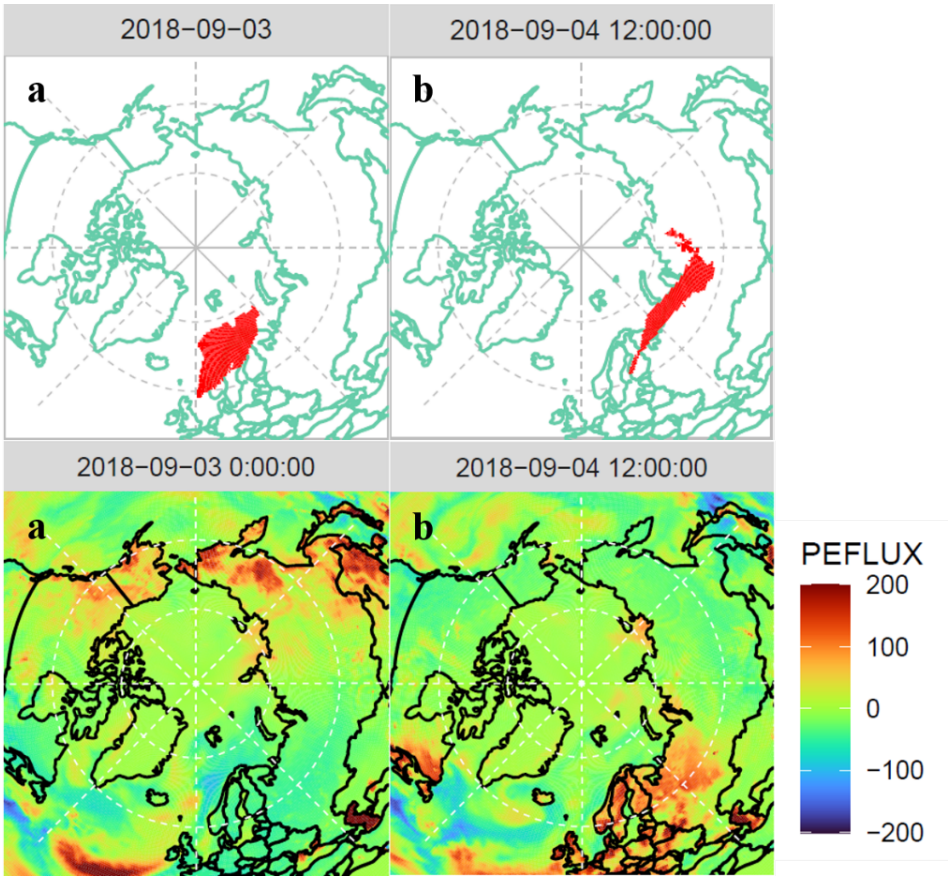

Fig. 15. Polar projections of AR basin (top, red shade) and heat maps of latent heat flux (bottom, unit in W/m^2) of the MERRA-2 AR 10234 event (2018-09-01 to 2018-09-05) at time step (a) 2018-09-03 0:00 and (b) 2018-09-04 12:00. At time step (a), latent heat flux in the detected AR basin was negative, indicating evaporation following AR intrusion over the ocean. When the AR moved into Europe at time step (b), latent heat fluxes of the AR basin and the surrounding coastal region became positive, which showed a massive precipitation as the AR made its landfall.

Similar to the latent heat fluxes, a prominent feature in sensible heat fluxes during an AR event was the strong negative values above the ocean (~ 100 W/m^2), but did not turn positive over land (Fig. 16). However, change in sensible heat flux kept declining in magnitude throughout the AR event. Unlike other parameters, sensible heat fluxes were highly impacted by the surrounding environment, so the change itself was not consistent across the AR basin, and could become undetectable when the AR moved into areas with strong background value.

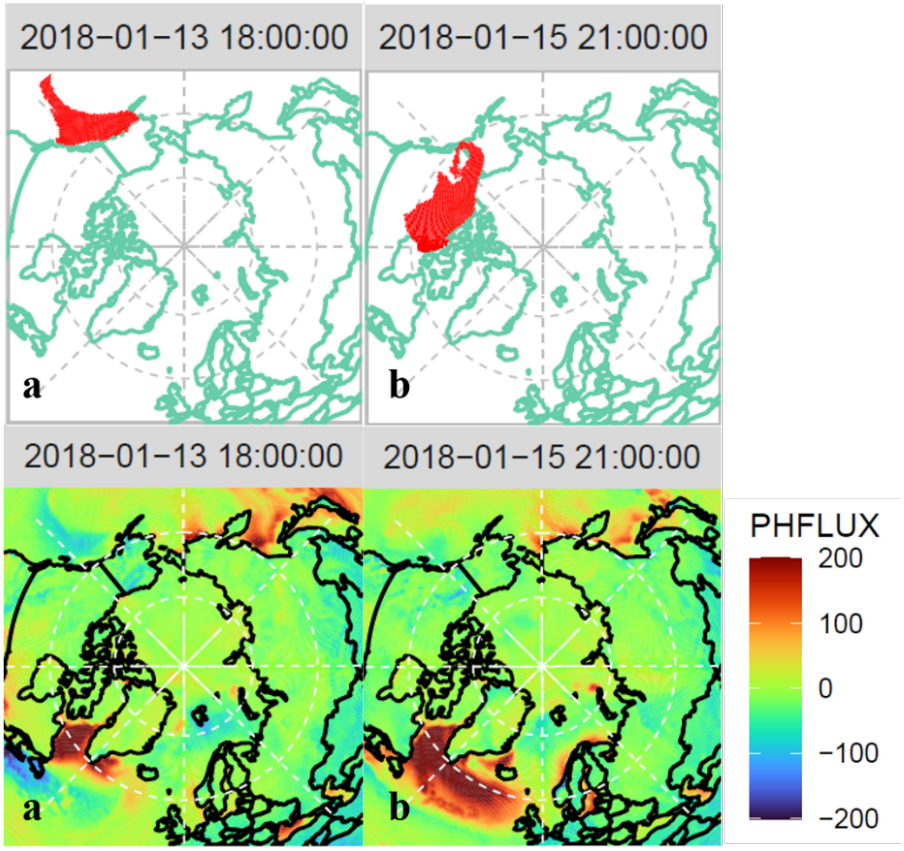

Fig. 16. Polar projections of AR basin (top, red shade) and heat maps of latent heat flux (bottom, unit in W/m^2) of the MERRA-2 AR 10440 event (2018-01-13 to 2018-01-17) at time step (a) 2018-01-13 18:00 and (b) 2018-01-15 21:00. At time step (a), sensible heat flux in the detected AR basin was negative, indicating heat flux moved from the surface to the atmosphere following AR intrusion over the ocean. When the AR moved into North America at time step (b), sensible heat fluxes of the AR basin did not shift to positive, yet, both the size and magnitude decreased through time. Please check Appendix I for details about AR basin, and Appendix II for details about sensible heat fluxes.

5. Discussions

5.1. Performance of AR indices

According to the plots of all 14 selected AR events, all variable except shortwave fluxes showed clear patterns that were correlated to the detected AR basins. Among all studied variables, the surface temperature was the best tool to characterize the evolving of the detected AR basin. The change in surface temperature were relatively consistent across the

whole AR basin as well as throughout the duration time of AR event. Since such temperature change remained the same along the track of ARs' movement and did not vary much after the AR basin expanded or contracted, it is easier to observe the range of AR's movement and the change in size of AR basin from the surface temperature plot. Geopotential at 1000 hPa, on the other hand, could be used to determine the relative location of the AR, since the low-pressure center was always in west or southwest to the AR basin. Although plots of heat fluxes and longwave fluxes did not clearly reveal the boundary or shape of detected AR basins, features could still be found corresponding to AR basins' movement, e.g., latent heat flux shifting to positive along the coastal line indicated the landfall of AR. Therefore, the climate time series Arctic AR index had a great performance in capturing the potential surface condition changes attributed to the Arctic AR events.

However, there were still limits on how to identify the AR using these variables. For instance, change in surface temperature was hard to be observe in the summer Arctic. And continents, especially the Eurasia, always had strong background signals that could affect the precision of projection plots. Since this project only removed the decadal mean from the MERRA-2 dataset, removing seasonal mean, monthly mean, or comparing across different simulation datasets (e.g., ERA5 dataset) could be considered for further research.

5.2. IWV vs. IVT

Two pairs of AR events (AR 10254 & 10661, AR 10234 & 10649) were selected to examine the performance of IWV & IVT AR indices. Each pairs contained AR basins detected by IWV and IVT indices for the same atmospheric river within the same duration time (IWV: AR 10254, 10234; IVT: AR 10661, 10649). The results showed that AR basins detected by IVT index were better at capturing features following the AR movement. For instance, the moving direction and expansion of low-pressure center favored the AR basin in AR event 10661 rather than AR event 10254 (Fig. 17). In this case, the low-pressure center was near the pole, when the IVT basin wandered around the central Arctic Ocean and IWV basin retreated all the way back to northern Europe. The longwave flux at top of

atmosphere pattern also had a better fit with the IVT basin, where the longwave flux profile was consistent with the AR basin's curving at the same location over Europe continent in AR event 10649 (Fig. 18). Thus, the IVT AR index was better at showing the motion of AR and the AR basin.

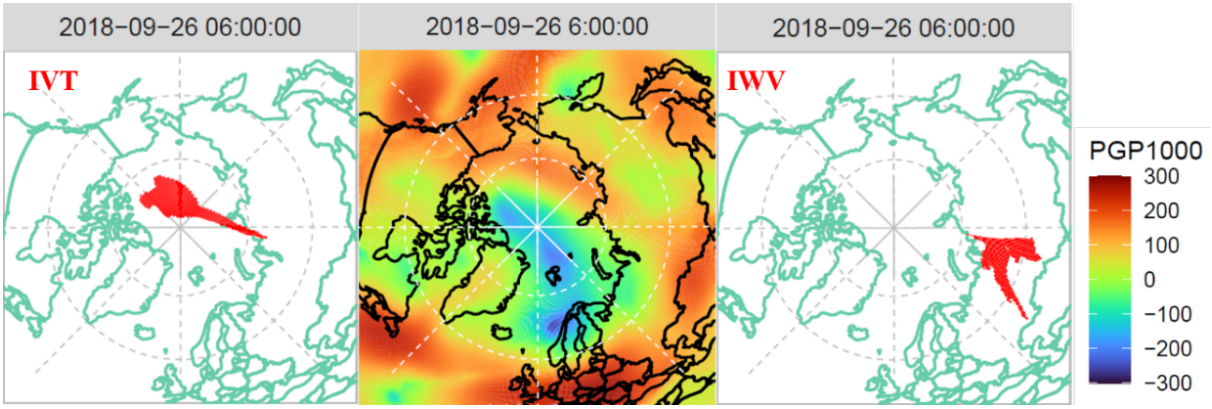

Fig. 17. Polar projections of AR basin using IVT AR index (left, red shade, AR 10661 event), heat map of geopotential at 1000 hPa (middle, unit in m), and Polar projections of AR basin using IWV AR index (right, red shade, AR 10254 event) at time step 2018-09-26 6:00. According to the geopotential heatmap, the low-pressure center was near the pole, which favored the movement of AR basin detected by the IVT AR index rather than the basin detected by IWV AR index. Please check Appendix I for details about AR event 10661 and 10254.

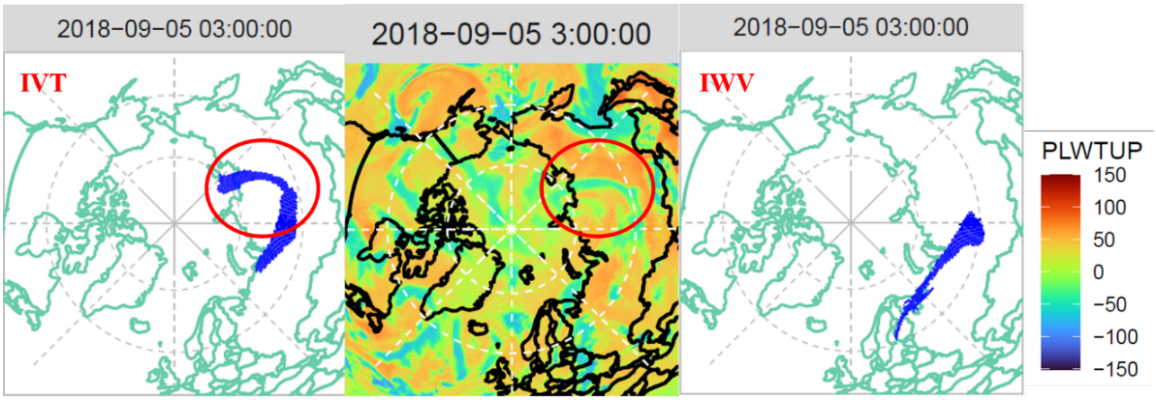

Fig. 18. Polar projections of AR basin using IVT AR index (left, red shade, AR 10649 event), heat map of upwelling longwave flux at top of atmosphere (middle, unit in W/m^2), and Polar projections of AR basin using IWV AR index (right, red shade, AR 10234 event) at time step 2018-09-05 3:00. According to the heatmap, the curving pattern of longwave flux over the northern Europe was similar to the IVT basin at the same location, when the IWV basin was still far away. Please check Appendix I for details about AR event 10649 and 10234.

5.3. Evaporation in the Arctic

Plots of latent heat flux showed a clear land-ocean difference in ARs' impact on the surface condition in the Arctic Ocean. Precipitation happened when ARs made the landfall was common and well accepted, but evaporation along with ARs were mostly observed in tropical areas (Algarra et al., 2020), as one of AR's significant roles was to bring warm moisture from low to high latitude. However, the plots of latent heat fluxes showed that the AR intrusion was not purely warm moisture from the low latitude, but also moisture from the Arctic itself. Some selected AR events, e.g., AR event 10021, had their AR basins above the Arctic Ocean over a week. Questions could be asked as what kind of mechanism that could maintain a consistent evaporation within such large area over a long duration time in the Arctic region? What kind of impact could the local moisture had on the atmospheric rivers during the evaporation? Whether the evaporation had positive feedback to the Artic Amplification? Also, evaporation was found to stop when the AR moved into central Arctic Ocean (Figure. 14), and cause of such feature was unclear. Future studies on moisture supply and temperature effect on evaporation status near the pole are needed to answer this question.

5.4. Greenhouse Effect

Surface temperature inside the AR basin was about 10 K higher than the decadal mean. Although such temperature increase was temporal and only exited during the AR event, a 10 K increase in surface temperature could enhance sea-ice melting in January and February, then provided positive feedback to the Arctic Amplification. According to plots of longwave fluxes, the net downward surface flux inside the AR basin was around 50 W/m^2 and the upwelling flux at top of atmosphere was about -100 W/m^2. Combining both results, the AR intrusion in the Arctic region results in about 50 W/m^2 more longwave fluxes going downward to the surface, and thus enhances the Greenhouse Effect. Besides, moisture being brought into the atmosphere by evaporation along with ARs could also act as a greenhouse gas, whose impact could be further amplified based on the size of the AR basin and the length of duration time. Thus, the AR intrusion did enhance the Arctic

Amplification and the AR indices were able to detect different mechanisms with the simulation datasets.

6. Conclusions

This project examined series of surface condition variables in 14 selected AR events in the Arctic, with AR basins detected by the MERRA-2 derived Arctic AR index. Both IWV & IVT indices had good performance in detecting the AR basins which correctly revealed changes in surface conditions caused by AR intrusions. The surface temperature had the best capability to characterize the evolving of detected AR basins, but it was only detectable during winter. Low-pressure center was found to be west to the AR basin through time for every AR event, and the increase in net downward longwave fluxes was observed corresponding to the AR basin as well. Latent and sensible heat fluxes showed consistent evaporation along with the AR basin over the Arctic Ocean, which could enhance the Greenhouse effect in the Arctic and the mechanism of this process remained in questions. Comparing to the IWV AR index, the IVT index performed better in capturing motion of ARs and detected AR basins. Seasonal effect and extreme background value over continents had highly impact on the result of analysis and should be considered for future studies. There are questions and hypothesis remain with the observation of surface conditions during the detected AR events, and more evidence and research are needed for further understanding the impact of AR on the Arctic region, its role in Arctic Amplification, and its associate physical mechanisms.

7. Acknowledgements

The author is grateful to Wen-wen Tung and Chen Zhang for the time series data of detected AR basins in the Artic (Tung et al., 2021; Zhang et al., 2021b) and their help on computing with data.

8. References

Algarra, I., Nieto, R., Ramos, A. M., Eiras-Barca, J., Trigo, R. M., & Gimeno, L. (2020). Significant increase of global anomalous moisture uptake feeding landfalling Atmospheric Rivers. *Nature Communications*, *11*(1), 1–7. https://doi.org/10.1038/s41467-020-18876-w

Baggett, C., Lee, S., & Feldstein, S. (2016). An investigation of the presence of atmospheric rivers over the North Pacific during planetary-scale wave life cycles and their role in Arctic warming. *Journal of the Atmospheric Sciences*, *73*(11), 4329–4347. https://doi.org/10.1175/JAS-D-16-0033.1

Cohen, J., Screen, J. A., Furtado, J. C., Barlow, M., Whittleston, D., Coumou, D., Francis, J., Dethloff, K., Entekhabi, D., Overland, J., & Jones, J. (2014). Recent Arctic amplification and extreme mid-latitude weather. *Nature Geoscience*, *7*(9), 627–637. https://doi.org/10.1038/ngeo2234

Crépin, A. S., Karcher, M., & Gascard, J. C. (2017). Arctic Climate Change, Economy and Society (ACCESS): Integrated perspectives. *Ambio*, *46*, 341–354. https://doi.org/10.1007/s13280-017-0953-3

Dufour, A., Zolina, O., & Gulev, S. K. (2016). Atmospheric moisture transport to the arctic: Assessment of reanalyses and analysis of transport components. *Journal of Climate*, *29*(14), 5061–5081. https://doi.org/10.1175/JCLI-D-15-0559.1

Gelaro, R., McCarty, W., Suárez, M. J., Todling, R., Molod, A., Takacs, L., Randles, C. A., Darmenov, A., Bosilovich, M. G., Reichle, R., Wargan, K., Coy, L., Cullather, R., Draper, C., Akella, S., Buchard, V., Conaty, A., da Silva, A. M., Gu, W., … Zhao, B. (2017). The modern-era retrospective analysis for research and applications, version 2 (MERRA-2). *Journal of Climate*, *30*(14), 5419–5454. https://doi.org/10.1175/JCLI-D-16-0758.1

Gimeno, L., Vázquez, M., Eiras-Barca, J., Sorí, R., Algarra, I., & Nieto, R. (2019). Atmospheric moisture transport and the decline in Arctic Sea ice. In *Wiley*

Interdisciplinary Reviews: Climate Change. https://doi.org/10.1002/wcc.588

Graversen, R. G., & Burtu, M. (2016). Arctic amplification enhanced by latent energy transport of atmospheric planetary waves. *Quarterly Journal of the Royal Meteorological Society*. https://doi.org/10.1002/qj.2802

Guan, B., Molotch, N. P., Waliser, D. E., Fetzer, E. J., & Neiman, P. J. (2010). Extreme snowfall events linked to atmospheric rivers and surface air temperature via satellite measurements. *Geophysical Research Letters*, *37*(20). https://doi.org/10.1029/2010GL044696

Hegyi, B. M., & Taylor, P. C. (2018). The Unprecedented 2016–2017 Arctic Sea Ice Growth Season: The Crucial Role of Atmospheric Rivers and Longwave Fluxes. *Geophysical Research Letters*, *45*(10), 5204–5212. https://doi.org/10.1029/2017GL076717

Johansson, E., Devasthale, A., Tjernström, M., Ekman, A. M. L., & L'Ecuyer, T. (2017). Response of the lower troposphere to moisture intrusions into the Arctic. *Geophysical Research Letters*, *44*(5), 2527–2536. https://doi.org/10.1002/2017GL072687

Komatsu, K. K., Alexeev, V. A., Repina, I. A., & Tachibana, Y. (2018). Poleward upgliding Siberian atmospheric rivers over sea ice heat up Arctic upper air. *Scientific Reports*, *8*(1). https://doi.org/10.1038/s41598-018-21159-6

Liu, Y., Key, J. R., Vavrus, S., & Woods, C. (2018). Time evolution of the cloud response to moisture intrusions into the Arctic during Winter. *Journal of Climate*, *31*(22), 9389–9405. https://doi.org/10.1175/JCLI-D-17-0896.1

Mix, H. T., Reilly, S. P., Martin, A., & Cornwell, G. (2019). Evaluating the roles of rainout and post-condensation processes in a landfalling atmospheric river with stable isotopes in precipitation and water vapor. *Atmosphere*, *10*(2), 1–13. https://doi.org/10.3390/ATMOS10020086

Naakka, T., Nygård, T., Vihma, T., Sedlar, J., & Graversen, R. (2019). Atmospheric moisture transport between mid-latitudes and the Arctic: Regional, seasonal and vertical distributions. *International Journal of Climatology*. https://doi.org/10.1002/joc.5988

Nash, D., Waliser, D., Guan, B., Ye, H., & Ralph, F. M. (2018). The Role of Atmospheric Rivers in Extratropical and Polar Hydroclimate. *Journal of Geophysical Research: Atmospheres*, *123*(13), 6804–6821. https://doi.org/10.1029/2017JD028130

NCAR CDG. (2019). *3-hourly MERRA2 IVT, uIVT, vIVT, IWV data computed for ARTMIP* (last access: 24 January 2019). https://doi.org/https://doi.org/10.5065/D62R3QFS

Nygård, T., Naakka, T., & Vihma, T. (2020). Horizontal moisture transport dominates the regional moistening patterns in the arctic. *Journal of Climate*, *33*(16), 6793–6807. https://doi.org/10.1175/JCLI-D-19-0891.1

Ralph, F. M., Wilson, A. M., Shulgina, T., Kawzenuk, B., Sellars, S., Rutz, J. J., Lamjiri, M. A., Barnes, E. A., Gershunov, A., Guan, B., Nardi, K. M., Osborne, T., & Wick, G. A. (2019). ARTMIP-early start comparison of atmospheric river detection tools: how many atmospheric rivers hit northern California's Russian River watershed? *Climate Dynamics*, *52*(7–8), 4973–4994. https://doi.org/10.1007/s00382-018-4427-5

Rutz, J. J., Shields, C. A., Lora, J. M., Payne, A. E., Guan, B., Ullrich, P., O'Brien, T., Leung, L. R., Ralph, F. M., Wehner, M., Brands, S., Collow, A., Goldenson, N., Gorodetskaya, I., Griffith, H., Kashinath, K., Kawzenuk, B., Krishnan, H., Kurlin, V., … Viale, M. (2019). The Atmospheric River Tracking Method Intercomparison Project (ARTMIP): Quantifying Uncertainties in Atmospheric River Climatology. *Journal of Geophysical Research: Atmospheres*, *124*(24), 13777–13802. https://doi.org/10.1029/2019JD030936

Shields, C. A., Rutz, J. J., Leung, L.-Y., Ralph, F. M., Wehner, M., Kawzenuk, B., Lora,

J. M., McClenny, E., Osborne, T., Payne, A. E., Ullrich, P., Gershunov, A., Goldenson, N., Guan, B., Qian, Y., Ramos, A. M., Sarangi, C., Sellars, S., Gorodetskaya, I., … Nguyen, P. (2018). Atmospheric River Tracking Method Intercomparison Project (ARTMIP): Project Goals and Experimental Design. *Geoscientific Model Development Discussions*, *January*, 1–55. https://doi.org/10.5194/gmd-2017-295

Sodemann, H., Wernli, H., Knippertz, P., Cordeira, J. M., Dominguez, F., Guan, B., Hu, H., Ralph, F. M., & Stohl, A. (2020). Atmospheric Rivers. *Atmospheric Rivers*. https://doi.org/10.1007/978-3-030-28906-5

Tung, W.-w., C. Zhang, Y. Huang, and W. S. Cleveland (2021). Climatology of Atmospheric Rivers and Associated Surface Warming in the Arctic: Tracking, Mean States, and Trends, *AGU Fall Meeting,* December 13-17, 2021.

Waliser, D., & Guan, B. (2017). Extreme winds and precipitation during landfall of atmospheric rivers. *Nature Geoscience*, *10*(3), 179–183. https://doi.org/10.1038/ngeo2894

Woods, C., & Caballero, R. (2016). The role of moist intrusions in winter arctic warming and sea ice decline. *Journal of Climate*, *29*(12), 4473–4485. https://doi.org/10.1175/JCLI-D-15-0773.1

Zhang, C., Tung, W., & Cleveland, W. S. (2021a). *In Search of The Optimal Atmospheric River Index for US Precipitation : A Multifactorial Analysis*. doi:10.1029/2020JD033667

Zhang, C., Tung, W., & Cleveland, W. S. (2021b). *Atlas of Arctic Atmospheric River Climatology Based on ERA5 and MERRA-2. Geophys. Res. Lett., in preparation.*

Zhu, Y., & Newell, R. E. (1998). A proposed algorithm for moisture fluxes from atmospheric rivers. *Monthly Weather Review*, *126*(3), 725–735. https://doi.org/10.1175/1520-0493(1998)126<0725:APAFMF>2.0.CO;2

9. Appendix Table of Contents

a. Appendix I (AR basins of 14 selected AR events in 2018)

FigureN18: Polar projection of total precipitable water vapor (shade, unit in kg/m^2) with wind at 850 hPa (vector, unit in m/s) for AR event 10469 at time step 2018-02-24 0:00 - Page 18